




## Superconducting contact and quantum interference between two-dimensional van der Waals and three-dimensional conventional superconductors

Michael R. Sinko <sup>1</sup>, Sergio C. de la Barrera <sup>1</sup>, Olivia Lanes,<sup>2</sup> Kenji Watanabe,<sup>3</sup> Takashi Taniguchi,<sup>3</sup> Susheng Tan <sup>4,5</sup>,  
David Pekker,<sup>2</sup> Michael Hatridge,<sup>2,\*</sup> and Benjamin M. Hunt<sup>1,†</sup>

<sup>1</sup>Department of Physics, Carnegie Mellon University, Pittsburgh, Pennsylvania 15213, USA

<sup>2</sup>Department of Physics and Astronomy, University of Pittsburgh, Pittsburgh, Pennsylvania 15260, USA

<sup>3</sup>Advanced Materials Laboratory, National Institute for Materials Science, Tsukuba, Ibaraki 305-0044, Japan

<sup>4</sup>Department of Electrical and Computer Engineering, University of Pittsburgh, Pittsburgh, Pennsylvania 15260, USA

<sup>5</sup>Petersen Institute of Nanoscience and Engineering, University of Pittsburgh, Pittsburgh, Pennsylvania 15260, USA



(Received 17 May 2020; accepted 19 November 2020; published 12 January 2021)

*This paper is a contribution to the joint Physical Review Applied and Physical Review Materials collection titled [Two-Dimensional Materials and Devices](#).*

Atomically thin two-dimensional (2D) transition-metal dichalcogenide (TMD) superconductors enable uniform, flat, and clean van der Waals tunneling interfaces, motivating their integration into conventional superconducting circuits. However, fully superconducting contact must be made between the 2D material and three-dimensional (3D) superconductors to employ the standard microwave drive and readout of qubits in such circuits. We present a method for creating zero-resistance contacts between 2D NbSe<sub>2</sub> and 3D aluminum that behave as Josephson junctions (JJs) with large effective areas compared to 3D-3D JJs. The devices formed from 2D TMD superconductors are strongly influenced by the geometry of the flakes themselves as well as the placement of the contacts to bulk 3D superconducting leads. We present a model for the supercurrent flow in a 2D-3D superconducting structure by a numerical solution of the Ginzburg-Landau equations and find good agreement with experiment. These results demonstrate a crucial step towards a new generation of hybrid superconducting quantum circuits.

DOI: [10.1103/PhysRevMaterials.5.014001](https://doi.org/10.1103/PhysRevMaterials.5.014001)

### I. INTRODUCTION

Superconducting circuits are ubiquitous in the field of quantum information. Typically fabricated by the deposition of metallic superconductors such as Al, Nb, or NbTiN, most superconducting qubits use Josephson junctions (JJs) whose tunnel barriers are created by *in situ* oxidation of aluminum electrodes [1,2]. Despite limitations associated with oxide thickness variability [3], aging, and absorption of molecules [3–5], JJ-based superconducting circuits are at the vanguard of quantum computing. They are used as state-of-the-art qubits but also employed in readout cavities, filters, amplifiers, and circulators. This is enabled by the ability to engineer desired nonlinear Hamiltonians, and by embedding junctions in a superconducting loop to form superconducting quantum interference devices (SQUIDs), as well as superconducting low-inductance undulatory galvanometers (SLUGs), superconducting nonlinear asymmetric inductive elements (SNAILS), and Josephson ring modulators (JRMs) [1,2,6–8].

Several designs of superconducting qubits require so-called super- or hyperinductances [9,10] which exhibit extreme protection from noise [11] and long coherence

times [9]. Kinetic inductance  $L_K$ , which results from the inertia of the charge carriers and is inversely proportional to cross-sectional area, is an alternate method for creating superinductances [12].  $L_K$  can be both large and precise in two-dimensional van der Waals (vdW) superconductors such as the transition-metal dichalcogenides (TMDs)  $2H_a$ -NbSe<sub>2</sub> and  $2H_a$ -TaS<sub>2</sub>, which can be exfoliated down to monolayers [13,14]. They also possess strong spin-orbit coupling, which leads to exceptionally high in-plane upper critical fields in few-layer devices [13,14]. This makes superinductances constructed from these materials ideal for hybrid experiments which use fluxonium qubits to detect and manipulate Majorana fermions in nanowires [15,16]. NbSe<sub>2</sub> and TaS<sub>2</sub> can also be readily incorporated in heterostructures in which hexagonal boron nitride (hBN) or semiconducting transition-metal TMDs replace oxides as significantly more stable, uniform, and atomically flat tunnel barriers [17–20].

In order to take advantage of these extraordinary properties, the most promising pathway is to integrate components built from two-dimensional (2D) vdW superconductors into conventional 3D superconducting circuits. The *sine qua non* of creating such a hybrid circuit is to create reliable, transparent, and robust superconducting contact between the 2D and 3D materials, minimizing dissipation and allowing the use of standard microwave drive and readout techniques. In this paper, we present such a method, demonstrating zero-resistance

\*hatridge@pitt.edu

†bmhunt@andrew.cmu.edu

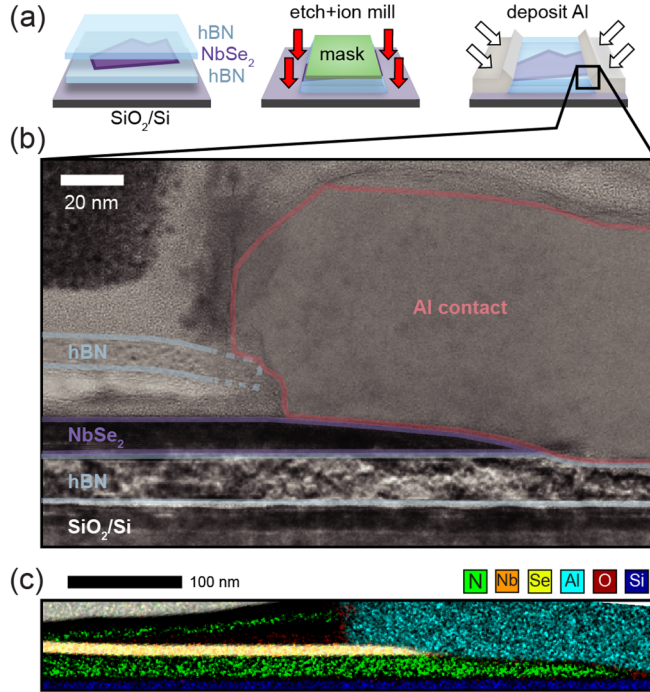


FIG. 1. Contact method and cross-sectional transmission electron microscopy (TEM). (a) Contact method. Thin  $\text{NbSe}_2$  is encapsulated by hBN. A reactive-ion etch exposes the  $\text{NbSe}_2$  edge. Following an *in situ* argon ion mill, contact is made using angled evaporation of aluminum with no adhesion layer. (b) Cross-sectional TEM of  $\text{NbSe}_2$ -Al interface in device F. (c) False-color energy dispersive spectroscopy (EDS) map of the  $\text{NbSe}_2$ -Al contact in device G. A slight delamination of the top hBN near the contact is visible, as in (b). Minimal oxygen is observed at the  $\text{NbSe}_2$ -Al contact.

contacts between 2D  $\text{NbSe}_2$  and 3D aluminum. We study the magnetic-flux response of devices having both two-terminal (3D-2D-3D) and SQUID geometries, demonstrating the unique character of the Josephson junction formed between 3D and intrinsic 2D superconductors. Aided by numerical solutions of the Ginzburg-Landau equations, we elucidate how the magnetic field response of 2D-3D superconducting devices depends strongly on the geometry of the 2D flake due to the gradual spatial variation of the screening currents in two dimensions.

## II. RESULTS AND DISCUSSION

We begin by describing our fabrication methods, shown in Fig. 1(a). Using exfoliation and standard dry-transfer techniques for stacking van der Waals materials inside a nitrogen-filled glove box [21], we encapsulate few-layer  $\text{NbSe}_2$  with hBN and contact the  $\text{NbSe}_2$  using evaporated aluminum with no intermediate adhesion layer, using a variation of the “edge contact” method [22] (Fig. 1). Briefly, we expose the edge of the  $\text{NbSe}_2$  by reactive-ion etching through all three layers of the hBN- $\text{NbSe}_2$ -hBN stack. We then transfer the stack immediately into an evaporation chamber for an argon ion mill process, to clean the exposed cross section of the stack, after which we tilt the sample *in situ* in the appropriate orientation to evaporate Al onto the exposed  $\text{NbSe}_2$  edge and

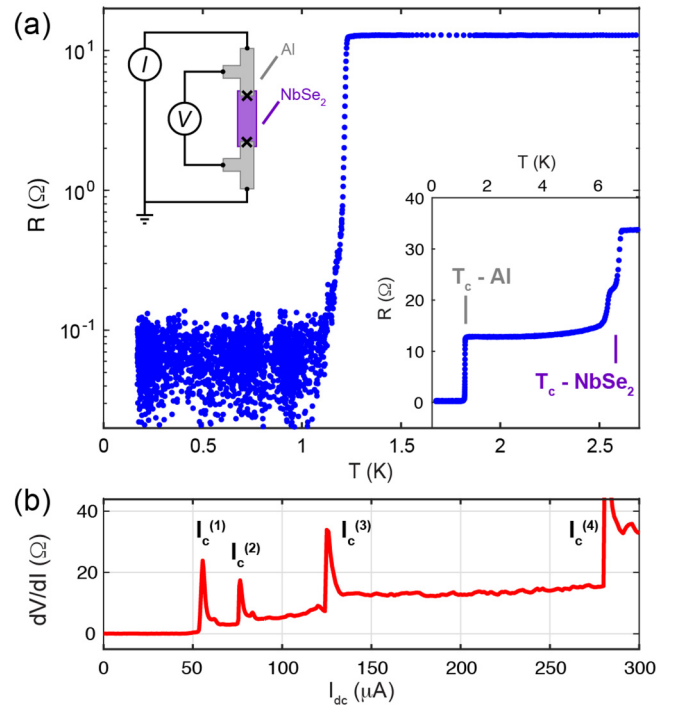


FIG. 2. Zero-resistance contact between few-layer  $\text{NbSe}_2$  and aluminum. (a)  $R(T)$  for Al- $\text{NbSe}_2$ -Al device F. Inset (bottom right): Linear plot of  $R(T)$  showing the Al and two  $\text{NbSe}_2$  transitions. Inset (top left): Four-point measurement setup for measuring the contact resistances of the Al/ $\text{NbSe}_2$  contacts. (b) Differential resistance ( $dV/dI$ ) vs dc current  $I_{dc}$  of device F, showing four dc critical currents. All measurements are filtered with low-pass and rf filters (Appendix C).

surface [Fig. 1(b) shows a cross-sectional TEM image of the result in one of our devices]. We have successfully made devices using both single- and double-angle evaporation.

A schematic of a two-terminal (3D-2D-3D) device is shown in the inset to Fig. 2(a). In the pseudo-four-terminal measurement configuration shown, the measured resistance  $R(T)$  is the series resistance of the 2D  $\text{NbSe}_2$  flake, the aluminum- $\text{NbSe}_2$  interface, and the 3D aluminum leads between the interface and the voltage probes. This measurement configuration allows us to eliminate resistances from the voltage and current leads, but includes the interface resistance between the 3D and 2D superconductors. Figure 2(a) shows a measurement of  $R(T)$  between 8 K and 175 mK. The transition at 7 K is that of the  $\text{NbSe}_2$  flake, whose  $T_c$  matches the bulk value of  $\text{NbSe}_2$ , reflecting a sample thickness of more than six layers [13]. A second transition occurring at 6.5 K is also associated with the  $\text{NbSe}_2$  flake, based on the temperature dependence of the critical current (Fig. 7). A final transition occurs at 1.2 K, which we attribute to the deposited aluminum leads as well as the Al/ $\text{NbSe}_2$  contacts. Below this final transition, the total resistance of the device, including the Al- $\text{NbSe}_2$  junctions, has dropped to zero within the noise floor of our measurement ( $R < 10^{-1} \Omega$ ). In the limit of  $T \rightarrow 0$ , four of five fully characterized devices (A, B, C, D, F) have a resistance of  $0.2 \Omega$  or less. The remaining devices have residual  $T \rightarrow 0$  resistances that range from a few  $\Omega$  up to  $81 \Omega$  (Table S1 [23] summarizes all studied devices).

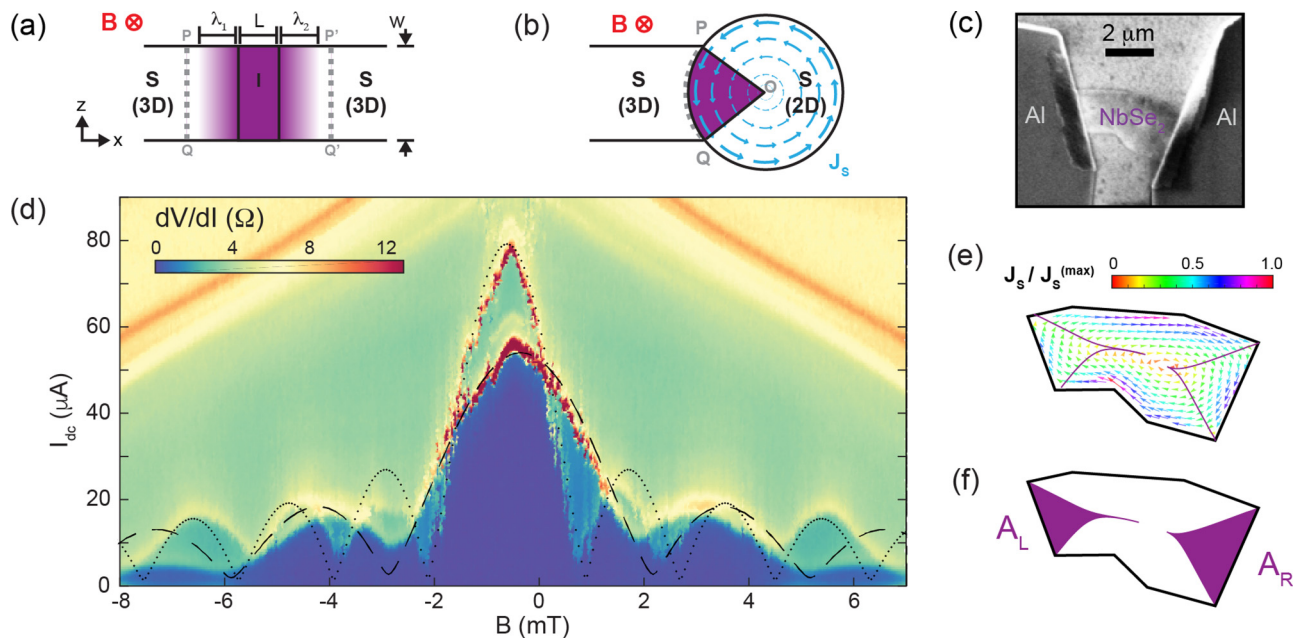


FIG. 3. Quantum interference in a two-terminal NbSe<sub>2</sub>-aluminum device. (a) Model of a 3D-3D Josephson junction. The phase difference  $\Delta\phi$  across the junction depends on the  $z$  coordinate.  $\Delta\phi_{PP'} - \Delta\phi_{QQ'}$  changes by  $2\pi$  when one  $\Phi_0$  of flux is threaded through the area depicted in magenta. (b) Model of a 2D-3D JJ. In response to a field  $\mathbf{B}$ , circulating supercurrent  $\mathbf{J}_s$  (blue arrows) flows in the 2D bulk. The phase difference across the junction winds by  $2\pi$  from point  $P$  to point  $Q$  when one  $\Phi_0$  is threaded through the effective area of the 2D-3D junction. This requires the effective area to be bounded by a contour of constant phase in the interior of the 2D flake,  $\overline{POQ}$ , perpendicular to  $\mathbf{J}_s$  everywhere. (c) Scanning electron microscopy (SEM) image of device F. (d)  $dV/dI$  as a function of  $I_{dc}$  and  $B$  for device F. Two superimposed single-junction critical current vs field  $I_c(B)$  responses are visible. Theoretical  $I_c(B)$  curves (black dotted and dashed lines) generated from the numerical simulations shown in E and F are overlaid on the data. Data for  $I_{dc} < 50 \mu\text{A}$  were acquired at 100 mK; slight heating occurs above  $50 \mu\text{A}$  but does not affect the analysis (Fig. 6). (e) Calculated supercurrent distribution  $\mathbf{J}_s$  and (f) effective areas  $A_L$  and  $A_R$  associated with the left and right contacts.

In Fig. 2(b), we plot the differential resistance ( $dV/dI$ ) as a function of the dc current  $I_{dc}$ . We observe four critical currents, of which the lower two show periodic modulations with applied magnetic field [Fig. 3(d)] while the larger two currents decrease monotonically with applied field (Fig. S3 [23]). This distinction associates the smaller two critical currents  $I_c^{(1)}$  and  $I_c^{(2)}$  with Josephson junctions hypothesized to occur at the Al/NbSe<sub>2</sub> interfaces, and the larger two critical currents  $I_c^{(3)}$  and  $I_c^{(4)}$  with the bulk Al and NbSe<sub>2</sub> respectively. We can distinguish the bulk Al and NbSe<sub>2</sub> critical currents by observing that  $I_c^{(3)} \rightarrow 0$  at  $T_c^{(\text{Al})} \sim 1$  K and  $I_c^{(4)} \rightarrow 0$  at  $T_c^{(\text{NbSe}_2)} \sim 7$  K. The two NbSe<sub>2</sub>-Al contacts in this device are slightly different in size [Table S1 [23] and Fig. 3(c)]; the narrower contact has  $I_c^{(1)} = 56.5 \mu\text{A}$  and the wider contact  $I_c^{(2)} = 78.5 \mu\text{A}$ , resulting in critical current densities  $J_c^{(1)} = 4.4 \times 10^8 \text{ A/m}^2$  and  $J_c^{(2)} = 4.96 \times 10^8 \text{ A/m}^2$ .

In Fig. 3(d), we plot the differential resistance of the same 3D-2D-3D device as in Fig. 2, as a function of  $I_{dc}$  and magnetic field perpendicular to the NbSe<sub>2</sub> plane,  $B$ . The data appear to display two interference patterns, suggesting that we are measuring a superposition of the individual responses from each junction. This is supported by our observation that in sequential data sets similar to Fig. 3(d), we have observed one set of peaks shifting relative to the other, likely due to the depinning of trapped flux at one of the contacts (Fig. S2 [23]).

In a 3D-3D superconducting JJ, the critical current  $I_c(B)$  is proportional to  $|\sin(x)/x|$  with the dimensionless flux  $x = \pi B A_{JJ} / \Phi_0$  penetrating the small area  $A_{JJ} = w \ell_{\text{eff}}$  of the barrier

region [Fig. 3(a)], where  $w$  is the width of the junction and  $\ell_{\text{eff}} = L + \lambda_1 + \lambda_2$  is given by the physical length  $L$  plus the penetration depths on either side of the junction,  $\lambda_1$  and  $\lambda_2$  [8]. Here,  $\Phi_0 = h/2e$  is the superconducting flux quantum. In our 2D-3D data [Fig. 3(d)], the two superimposed interference patterns have oscillation periods  $\Delta B_i \approx 2$  and  $4$  mT, corresponding to JJ areas  $A_{\text{meas}} = \Phi_0 / \Delta B_i$  of  $1$  and  $0.5 \mu\text{m}^2$ , respectively. These areas are 10%–20% of the total NbSe<sub>2</sub> flake area and, importantly, are significantly larger than the equivalent area  $A_{\text{geom}}$  produced by our contact method. From Figs. 1(b) and 3(c),  $A_{\text{geom}}$  has a conservative upper bound of  $\sim 0.1 \mu\text{m}^2$ , resulting in a lower bound of  $A_{\text{meas}}/A_{\text{geom}} \sim 7$  and  $10$  for the two contacts (Table I). It is

TABLE I. Select properties of four devices. More comprehensive data including three additional devices are in Table S1 [23].  $A_{\text{meas}}/A_{\text{geom}}$  is the factor by which the device area measured from quantum interference exceeds that deduced from the geometry, and is explained further in the main text.  $A_{\text{meas}}/A_{\text{geom}}$  refers only to the SQUID-like contact for devices B and C and to both 2D-3D contacts for devices A and F.

Device	A	B	C	F
Geometry	Two terminal	SQUID	SQUID	Two terminal
Thickness (nm)	10	11.2	11.3	11.9
$I_c$ ( $\mu\text{A}$ )	12, 26	10, 40	0.15, 3	56.5, 78.5
$A_{\text{meas}}/A_{\text{geom}}$	9, 8.7	3.5	2.7	7, 10



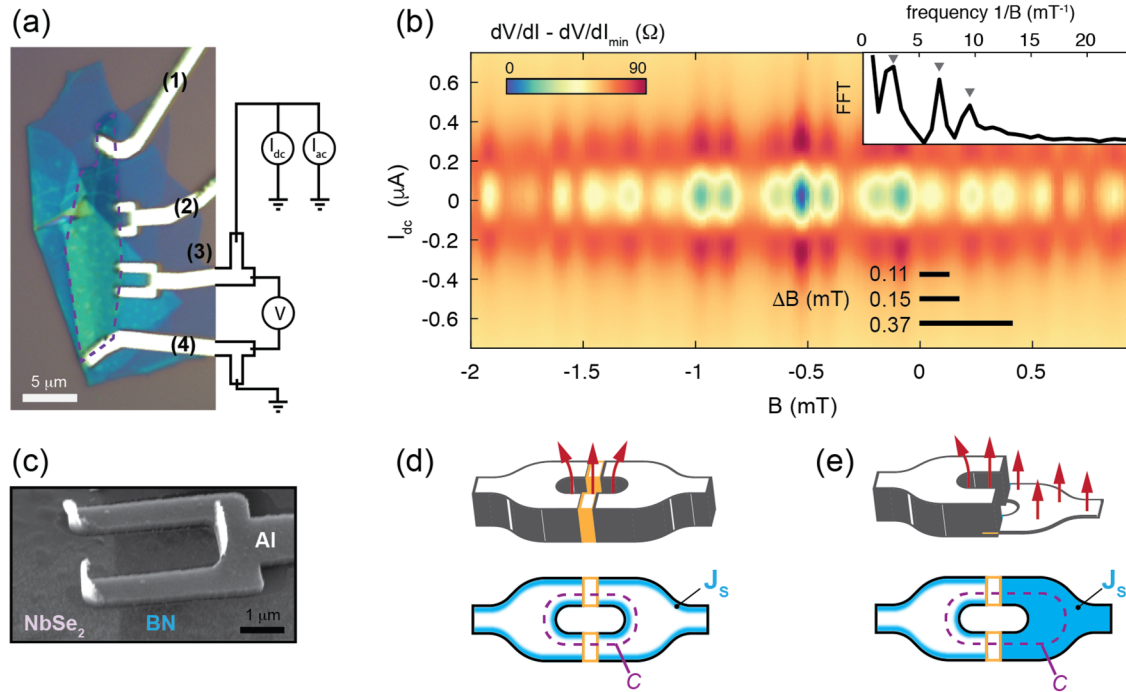


FIG. 4. Quantum interference in a 2D-3D NbSe<sub>2</sub>-aluminum SQUID. (a) Optical micrograph of device C.  $dV/dI$  measurements are performed between contacts No. 3 and No. 4 while contacts No. 1 and No. 2 are floating. Outline of NbSe<sub>2</sub> flake is shown in dashed purple line. (b) Quantum interference pattern observed in device C. A minimum resistance of  $(dV/dI)_{\min} = 81 \Omega$  has been subtracted from the data. Data for SQUID device B (Fig. S5 [23]) show a true zero resistance as  $T \rightarrow 0$ . Inset: Fast Fourier transform (FFT) amplitude of a linecut along  $I_{dc} = 0$  (the following results do not depend on chosen  $I_{dc} = 0$ ). The three frequencies, indicated by arrows, are  $1/\Delta B_i = 2.7, 6.8,$  and  $9.5 \text{ mT}^{-1}$  (corresponding respectively to periods  $\Delta B_i = 0.37, 0.15,$  and  $0.11 \text{ mT}$ , shown as black scale bars in the main figure, and areas  $A_{\text{meas}}^{(i)} = \Phi_0/\Delta B_i = 5.4, 13.6,$  and  $19.1 \mu\text{m}^2$ ). The lowest and highest of these areas match the calculated effective areas of the SQUID source and 2D-3D drain contacts. (c) SEM image of the SQUID “source” contact in device C formed by two Al contacts to the NbSe<sub>2</sub> flake. (d) In a 3D-3D SQUID, the supercurrent  $\mathbf{J}_s$  flows in a surface layer of depth  $\sim \lambda$ . The fluxoid quantization contour  $C$  can be chosen deep in the interior of the superconductor such that  $\int_C \mathbf{J}_s \cdot d\ell = 0$ . (e) In a 2D-3D SQUID, since  $\mathbf{J}_s$  is nonzero everywhere in the 2D layer,  $C$  must be a contour of constant phase inside the bulk, which results in a larger effective area determining the periodicity of  $I_c(B)$  oscillations.

worth noting that a Fraunhofer-like interference pattern in a typical 3D-3D JJ is typically not observed experimentally because  $A_{JJ}$  is sufficiently small that one period of the oscillation  $\gg H_{c2}$  of aluminum, highlighting the distinct behavior of our 2D-3D JJ.

In a 2D superconductor of thickness  $d \ll \lambda$ , where  $\lambda$  is the penetration depth, the relevant length scale for the screening of the applied field is the Pearl length  $\lambda_{\text{Pearl}} = 2\lambda^2/d$  [24]. For screening currents in the NbSe<sub>2</sub> plane,  $\lambda = 124 \text{ nm}$  [25], giving  $\lambda_{\text{Pearl}} = 2.6 \mu\text{m}$  for 11.9-nm-thick device F.  $\lambda_{\text{Pearl}}$  is thus comparable to or can exceed the size of the sample for very thin flakes and the magnetic flux nearly uniformly penetrates the superconductor. In comparison to the 3D-3D JJ, the effective area penetrated by the flux is much larger in the 2D-3D junction, and the contour around which the superconducting phase winds by  $2\pi$  is determined by the specific flow pattern of the supercurrent  $\mathbf{J}_s$  in the 2D flake [Fig. 3(b)]. In contrast to 3D London superconductors, the path of this contour in the 2D flake is unique, giving rise to a strong sensitivity of the interference pattern to the precise shape and size of the 2D flake as well as to the placement of the 3D leads. To understand quantitatively the shorter oscillation periods (larger areas) seen in the Fig. 3 data, we constructed a theoretical model for the flow of supercurrent  $\mathbf{J}_s$  in our device, based on numerical solutions of the Ginzburg-Landau equations (Appendix A). We emphasize

that the only input to our numerical model is the geometry of the 2D NbSe<sub>2</sub> flake. The results of the simulation for both contacts are shown in Figs. 3(e) and 3(f), and the  $I_c(B)$  for both contacts are superimposed on the data in Fig. 3(d). With only the flake shape as an input parameter, our simple model does a good job of explaining the critical currents: The ratio of the central peak to the satellite peaks is quite accurate, and the predicted areas are within about 8% of the values measured in the experiment. Additionally, our model predicts that the critical currents do not reach zero, a feature of the experimental data as well. Critical current zeros occur when forward and backward supercurrents across the junction perfectly cancel each other, which would not be expected for our flakes due to a lack of mirror symmetry with respect to a line perpendicular to the JJ that bisects it into two equal segments. Agreement between simulation and experiment might be improved here if we relaxed our assumption of uniform Josephson coupling along the interface.

We also studied devices consisting of a SQUID-loop “source” contact [Fig. 4(a), contact No. 3] in series with a 2D-3D “drain” contact (contact No. 4). The critical current [Fig. 4(d)] shows oscillations periodic in magnetic field; a Fourier transform of the data in Fig. 4(b) reveals three frequencies  $1/\Delta B_i = 2.7, 6.8,$  and  $9.5 \text{ mT}^{-1}$ , which correspond respectively to areas  $A_{\text{meas}}^{(i)} = \Phi_0/\Delta B_i = 5.4, 13.6,$  and

$19.1 \mu\text{m}^2$ . None of these precisely matches the physical area of the SQUID shown in detail in Fig. 4(c) ( $A_{\text{geom}} = 7 \mu\text{m}^2$ ) and the beating pattern is inconsistent with the ratio of SQUID area to Josephson junction area. Employing our theoretical model, we calculated the effective areas of both the SQUID source and 2D-3D drain contacts. The effective area  $A_{\text{eff}}$  of the SQUID, bounded by the unique contour around which the superconducting phase winds by  $2\pi$ , is larger than that of the physical area due to the contribution of nonzero  $\mathbf{J}_s$  flowing in the bulk of the 2D flake [Fig. 4(e)]. We find that the effective SQUID area is  $A_{\text{eff}} = 19.7 \mu\text{m}^2$ , very close to the experimentally determined value of  $19.1 \mu\text{m}^2$  calculated from the largest frequency,  $1/\Delta B = 9.5 \text{ mT}^{-1}$ . The drain contact behaves as a 2D-3D JJ with a large effective area, similar to the two-terminal device in Fig. 3; our simulation predicts  $A_{\text{eff}} = 6.3 \mu\text{m}^2$ , which corresponds to the lowest observed frequency  $1/\Delta B = 2.7 \text{ mT}^{-1}$  ( $5.4 \mu\text{m}^2$ ). Our observation of a third frequency has no straightforward explanation using our model, but may be related to coupling between phase slips on the two junctions, mixing the frequencies and giving rise to additional sum/difference frequencies. A second SQUID (device B, Fig. S5 [23]) also shows a measured effective area much larger than the physical loop area of the device  $A_{\text{meas}}/A_{\text{geom}} \approx 3.5$ .

### III. CONCLUSION

In conclusion, we have shown that robust superconducting contacts can be made between 2D TMD intrinsic superconductors and conventionally deposited 3D metals. These contacts form Josephson junctions between two dissimilar superconductors, whose oscillation period in  $I_c(B)$  suggests that the effective flux-sensitive areas  $A_{\text{meas}}$  of the Josephson junctions are significantly larger than the expected areas  $A_{\text{geom}}$ . The  $\sim \mu\text{m}^2$  effective areas of our JJs suggests that they may be useful in a novel scanning magnetometer because, due to large  $A_{\text{meas}}/A_{\text{geom}}$ , they could combine a small geometric area—enabling high spatial resolution—with the flux sensitivity of a larger JJ. Moreover, the object on the end of the scanning tip would be a single 2D-3D JJ, simplifying the magnetometer design compared to state-of-the-art scanning SQUID microscopes [26]. Our demonstration of Josephson coupling with an *edge-on* geometry between an *s*-wave superconductor and atomically thin NbSe<sub>2</sub> is a crucial step toward direct phase-sensitive measurements of the pairing symmetry in the latter, which may possess odd-parity components leading to exotic properties such as nodal and topological superconductivity [27,28], and has recently shown an unexpected anisotropy of the order parameter in vertical tunneling experiments [29]. Such measurements were instrumental in revealing *d*-wave symmetry in the cuprates [30]. Finally, these 2D-3D superconducting contacts lay the foundation of a technological pathway to integrate 2D vdW superconductors as novel components, such as superinductance-based qubits, in conventional 3D aluminum-based superconducting circuits.

### IV. OUTLOOK

Two-dimensional van der Waals materials and three-dimensional aluminum-based superconducting circuits have

been two extremely popular areas of research in recent years, the former because of the countless new devices and designer materials enabled by the van der Waals architecture, and the latter because of its central role in superconductor-based quantum information processing. We envision that our advance—the ability to graft 2D superconductors onto 3D aluminum with zero-resistance and high-critical-current contacts—will be among the first steps in harnessing the properties of atomically-thin materials for use in the circuit quantum electrodynamics (cQED) architecture. We imagine that the ability to join 2D and 3D superconductors will facilitate the integration of such components as vertical Josephson junctions based on stable, oxide-free tunnel barriers or lateral, gate-defined junctions; superinductances based on the kinetic inductance of single-layer superconductors; physically compact, field-tolerant transmon qubits based on few-layer-thick, crystalline capacitors; and components based on high-temperature and topological superconductors.

### ACKNOWLEDGMENTS

Work on device fabrication and measurement by M.R.S. and O.L. was supported by the National Science Foundation PIRE program under Award No. 1743717. B.M.H. acknowledges support by the Department of Energy under the Early Career award program (DE-SC0018115). S.C.B. was supported by the Department of Energy (DE-SC0018115) for measurements of the superconducting devices. B.M.H. and S.C.B. acknowledge support in the early stages of this project from the Charles E. Kaufman Foundation, a supporting organization of The Pittsburgh Foundation, via Young Investigator Research Grant No. KA2016-85226. B.M.H. acknowledges additional support from the Research Corporation for Science Advancement through a Cottrell Scholar Award No. (26005). The authors acknowledge use of the Materials Characterization Facility at Carnegie Mellon University supported by Grant No. MCF-677785. This work was performed, in part, at the Nanoscale Fabrication and Characterization Facility, a laboratory of the Gertrude E. and John M. Petersen Institute of NanoScience and Engineering, housed at the University of Pittsburgh. We also thank the Pittsburgh Quantum Institute (PQI) for hosting many productive conversations.

### APPENDIX A: THEORETICAL MODEL

In this Appendix we build a model for the dependence of the Josephson current between the aluminum leads and the NbSe<sub>2</sub> flake, similar in spirit to Ref. [31]. We make the assumption that the Josephson energy  $E_J$  of the contact between the leads and the flake is much lower than the energy of the screening supercurrents induced by the magnetic field in the flake. For a JJ with  $I_c = 75 \mu\text{A}$ ,  $E_J = \Phi_0 I_c / 2\pi \approx 150 \text{ meV}$ . The energy of the screening supercurrents is roughly two orders of magnitude higher, with the reasonable assumptions that the (2D) superfluid density is  $n_s \sim 10^{15} \text{ cm}^{-2}$  and that the phase gradient in the sample is of the order of  $2\pi/L$ , where  $L \sim 2 \mu\text{m}$  is a linear dimension of the 2D sample. This assumption significantly simplifies our analysis as we can first build a model of the supercurrents in the flake and then use the output of this model to obtain the Josephson currents.

Our starting point for describing the supercurrents in the flake is the Ginzburg-Landau equation

$$\alpha\psi + \beta|\psi|^2\psi + \frac{1}{2m^*} \left( \frac{\hbar}{i} \vec{\nabla} - \frac{2e}{c} \vec{A} \right)^2 \psi = 0, \quad (\text{A1})$$

where  $\psi$  is the complex order parameter,  $\vec{A}$  is the gauge field,  $m^*$  is the mass of a Cooper pair, and  $\alpha$  and  $\beta$  the Landau-Ginzburg parameters. For small superconductors (such that the linear size of the 2D sample is much smaller than the Pearl penetration depth) the magnetic field completely penetrates the superconductor, and hence one can ignore the variations in the magnitude of  $\psi$ . Therefore, we express the order parameter  $\psi$  in terms of a (constant) amplitude  $\psi_0$  and a position dependent phase  $\phi(\vec{r})$ :  $\psi(\vec{r}) = \psi_0 e^{i\phi(\vec{r})}$ . Using this form of the order parameter, the Ginzburg-Landau equation becomes

$$\vec{\nabla}^2 \phi(\vec{r}) - \frac{2e}{\hbar c} \vec{\nabla} \cdot \vec{A}(\vec{r}) = 0. \quad (\text{A2})$$

The supercurrents are given by

$$\vec{J}(\vec{r}) = \frac{2e\hbar}{m^*} \psi_0^2 \left( \vec{\nabla} \phi(\vec{r}) - \frac{2e}{\hbar c} \vec{A}(\vec{r}) \right). \quad (\text{A3})$$

To obtain the current distribution in the flake we numerically solve Eq. (A2) subject to the boundary condition that there is no supercurrent across the boundary, i.e.,  $\vec{J} \cdot \vec{n}|_{\partial} = 0$ , where  $\vec{n}$  is the unit normal vector on the boundary. We note that in principle the current across the boundary should be nonzero in the regions of contact between the flake and the aluminum leads. We ignore this contribution following our assumption of weak Josephson currents. We also note that Eq. (A2) (supplemented by the boundary conditions) is linear  $\phi(\vec{r}) \propto B_z$ , and hence it is sufficient to obtain  $\phi(\vec{r})$  for a single value of  $B_z$  and then scale the resulting solution.

To obtain numerical solutions, we wrote a *Mathematica* script which allows us to trace the shape of the flake and convert it into a partial differential equation for  $\phi(\vec{r})$  supplemented by Neumann boundary conditions (we use the Landau gauge  $\vec{A}(\vec{r}) = B_z x \hat{e}_y$ ). The computed supercurrents in the flake are plotted in Fig. 3(e).

To compute the Josephson current between the  $i$ th lead and the flake we define the phase

$$\chi = \varphi + \int dl \left( \vec{\nabla} \phi(\vec{r}) - \frac{2e}{\hbar c} \vec{A}(\vec{r}) \right), \quad (\text{A4})$$

where  $\varphi$  is the superconducting phase associated with the flake and the integral runs around the boundary of the flake. The Josephson current between the  $i$ th lead and the flake is given by

$$J_i = J_c \int_{\text{contact}} dl \sin(\phi_i - \chi), \quad (\text{A5})$$

where  $J_c$  is the critical current density,  $\phi_i$  is the superconducting phase of the  $i$ th lead, and the line integral runs over the points at which the lead makes contact with the flake.

## APPENDIX B: DEVICE FABRICATION

We fabricate devices by exfoliating  $\sim 10$ - $\mu\text{m}$ -long flakes from a bulk crystal of  $2H$ -NbSe<sub>2</sub> sourced from HQ Graphene. Intrinsically superconducting TMDs are air and water vapor

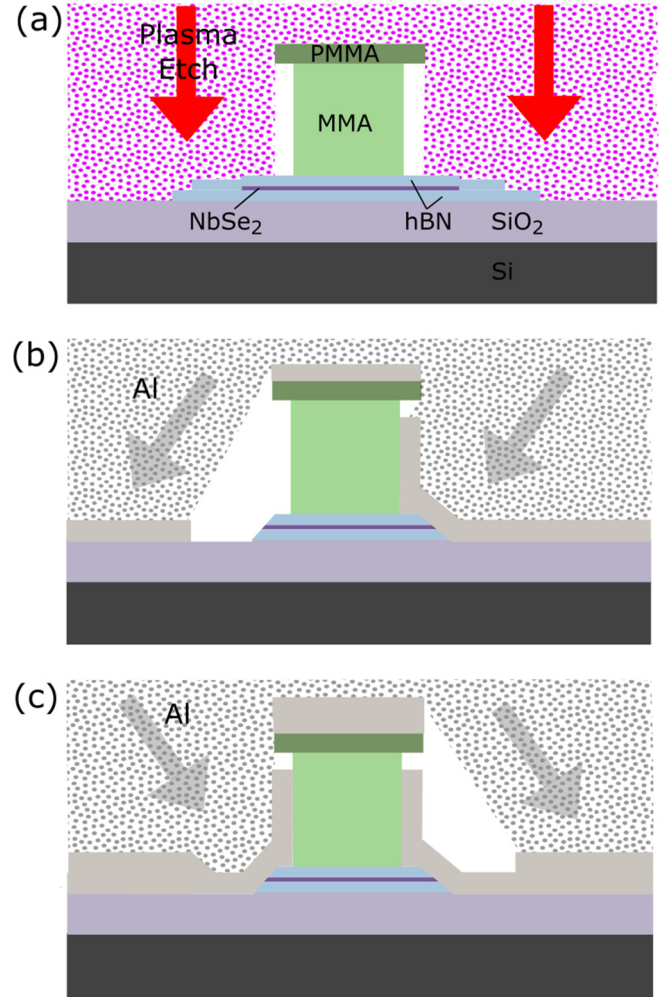


FIG. 5. (a) After the lithographic mask is patterned via electron-beam lithography (EBL), a reactive-ion etch is used to expose a cross section of the hBN/NbSe<sub>2</sub>/hBN heterostructure. The stack is then loaded into a Plassys 8-pocket e-gun evaporator with an ion gun where a 3-min Ar ion mill step is used to expose a fresh facet *in situ* before evaporation. (b) Aluminum is evaporated at an angle 30° from vertical. (c) Optionally, additional evaporation angles can be used, but will result in additional aluminum critical currents due to the layering [see Figs. S4(b) and S4(c) [23]].

sensitive and begin to degrade in an ambient environment. This necessitates the encapsulation of NbSe<sub>2</sub> by hBN, which we perform using standard dry transfer techniques in an inert N<sub>2</sub> glove-box environment to prevent the degradation of the air-sensitive NbSe<sub>2</sub>. After a poly(methyl methacrylate)/methyl methacrylate (PMMA/MMA) bilayer resist mask is patterned using e-beam lithography, an initial etch is made with CHF<sub>3</sub>/O<sub>2</sub> in a reactive-ion etching system. (See Fig. 5.)

The sample is examined and then sealed in an inert environment until it is loaded into a Plassys 8-pocket e-gun evaporator with an ion gun. An initial 3-min, high-power Ar ion mill step is used to clean and expose fresh surfaces on the exposed cross sections of the heterostructure, then the substrate is rotated to an angle  $\pm 30^\circ$  from perpendicular to the direction of evapo-



ration. This angle ensures thorough coverage of the exposed NbSe<sub>2</sub> cross section by the Al, evaporated at 0.3 nm/s.

Al is evaporated to ensure uniform coverage of heterostructures that range from 30 to 60 nm, devices with leads facing opposite directions have 40 nm deposited while the sample is tilted to one side, and then another 40 nm of Al deposited while it is tilted in the opposite direction. We have not conclusively identified the origin of the nonzero resistances in some devices, but as we have improved our device fabrication procedures, particularly the *in situ* ion milling immediately prior to Al evaporation, the yield of  $R = 0$  devices has increased from  $\sim 20\%$  for our earliest attempts to  $\sim 50\%$  for our most recent samples and has also resulted in consistently higher critical current densities.

### APPENDIX C: MAGNETOTRANSPORT MEASUREMENTS

Magnetotransport measurements were performed using standard low-frequency ac lock-in techniques with an SR860 lock-in amplifier sourcing 100 mV through a 1 M $\Omega$  bias resistor and the RC filters producing a 98 nA excitation current (Fig. 6). The dc currents were sourced from a Keithley 2400 source measure unit (SMU) through a 10 M $\Omega$  bias resistor (alternatively using a Yokogawa GS200 SMU as a dc current source). No qualitative differences were observed in the signals when measured using excitation currents of 9.8 or 0.98 nA.

The devices were measured in a dilution refrigerator to a minimum temperature of 40 mK in fields up to 5 T. Figure 2(a) (inset) schematically shows the measurement setup in which each superconducting lead that connects to the NbSe<sub>2</sub> flake splits in two, enabling a four-point resistance measurement that would isolate any remaining contact resistance after both

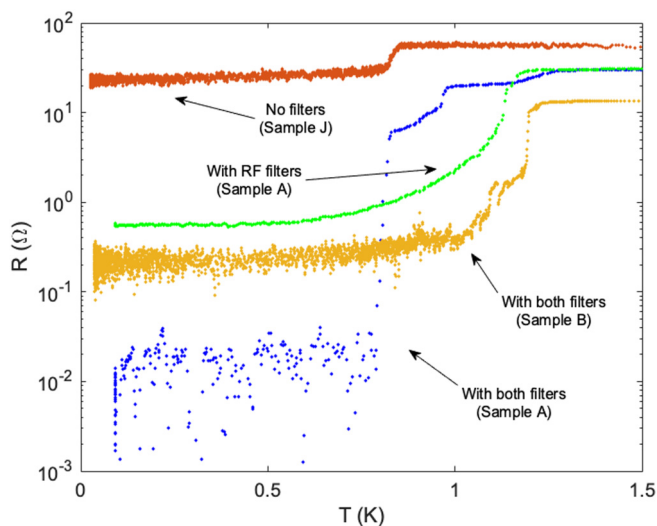


FIG. 6. Comparison of  $R(T)$  plots of devices A and B measured with filters, and device J (not listed in Table S1) without any filters used in the measurement. The curve from Fig. S4(a) is reproduced and compared with a measurement on the same device using only rf filters with a cutoff frequency in the GHz regime.  $R(T)$  for the SQUID device B with all filters in place shows a residual resistance two orders of magnitude lower than that of device J without filters, but unlike device A, the resistance remains nonzero.

the Al lead and NbSe<sub>2</sub> flake have transitioned to superconducting states.

A series of filters were used to isolate the device from high-frequency noise, including a low-pass RC filter, Cu tape, GHz filters, and a Cu clamshell enclosure, serving as a Faraday cage to encase and isolate the device [32–36]. These filters block higher-frequency noise that drives the contact out of the superconducting state, creating a residual resistance [32]. The resistive noise floors at the base temperature shown in Figs. 2(a) and S4(a) correspond to  $V_{\text{rms}} = 6.7$  and 0.8 nV respectively, using an integration time of 3 s to acquire the  $R = 0$  data.  $dV/dI$  measurements were taken by sweeping the sourced dc current at stepped field intervals to form the color plot in Fig. 4(b).

Larger dc currents caused Joule heating in the RC low-pass filters mounted directly adjacent to the device, so the sample temperature increases slightly with increasing dc current. While the heating does not approach or exceed any of the critical temperatures, the elevated temperature does slightly depress critical currents in several measurements, however, because the device only begins to heat above base temperature at  $I_{\text{dc}} = 50 \mu\text{A}$  our analysis of each interference pattern periodicity is unaffected. This heating raises the device temperature to 150 mK at  $I_{\text{dc}} = 80 \mu\text{A}$  and 300 mK at  $I_{\text{dc}} = 120 \mu\text{A}$ . This can be seen most clearly in Fig. 7(b) where

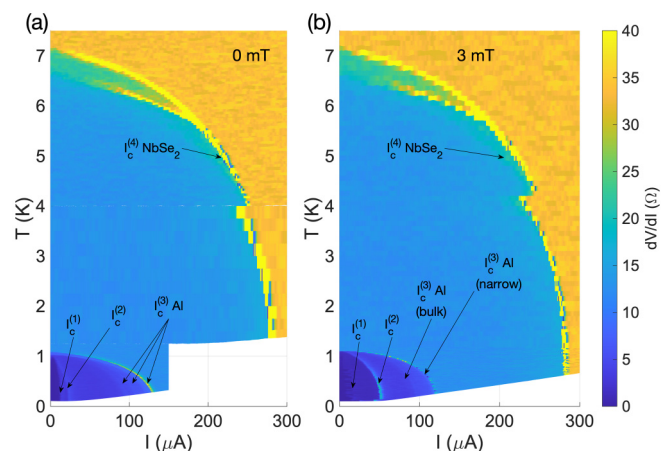


FIG. 7. (a)  $dV/dI$  vs  $T$  and  $I_{\text{dc}}$  at 0 mT (device F). The critical currents associated with the contacts ( $I_c^{(1)}$  and  $I_c^{(2)}$ ) are well below their maximum at zero flux, indicating that this measurement with zero applied field is measuring a finite amount of trapped flux through the NbSe<sub>2</sub> flake in the areas associated with each junction. (b)  $dV/dI$  vs  $T$  and  $I_{\text{dc}}$  at 3 mT. The smaller of the critical currents (associated with the narrower of the two contacts) exhibits hopping behavior between two discrete flux states. This suggests that a single vortex is moving in and out of the area of the NbSe<sub>2</sub> flake measured by this contact. The shift in  $I_c$  between the two levels is significant. In both plots, the  $T_c$  of all critical currents associated with the aluminum leads and Al/NbSe<sub>2</sub> contacts is 1.2 K. Above 5.5 K the NbSe<sub>2</sub> critical current splits into two critical currents with  $T_c = 6.5$  and 7 K. Note: The discontinuity in  $I_c^{(4)}$  (NbSe<sub>2</sub>) at 4 K is attributed to the different heating behavior of the cryogen-free dilution refrigerator above and below 4 K, and the positive slope of the color plots' lower boundaries show the inaccessible temperature region due to Joule heating at larger  $I_{\text{dc}}$  values.

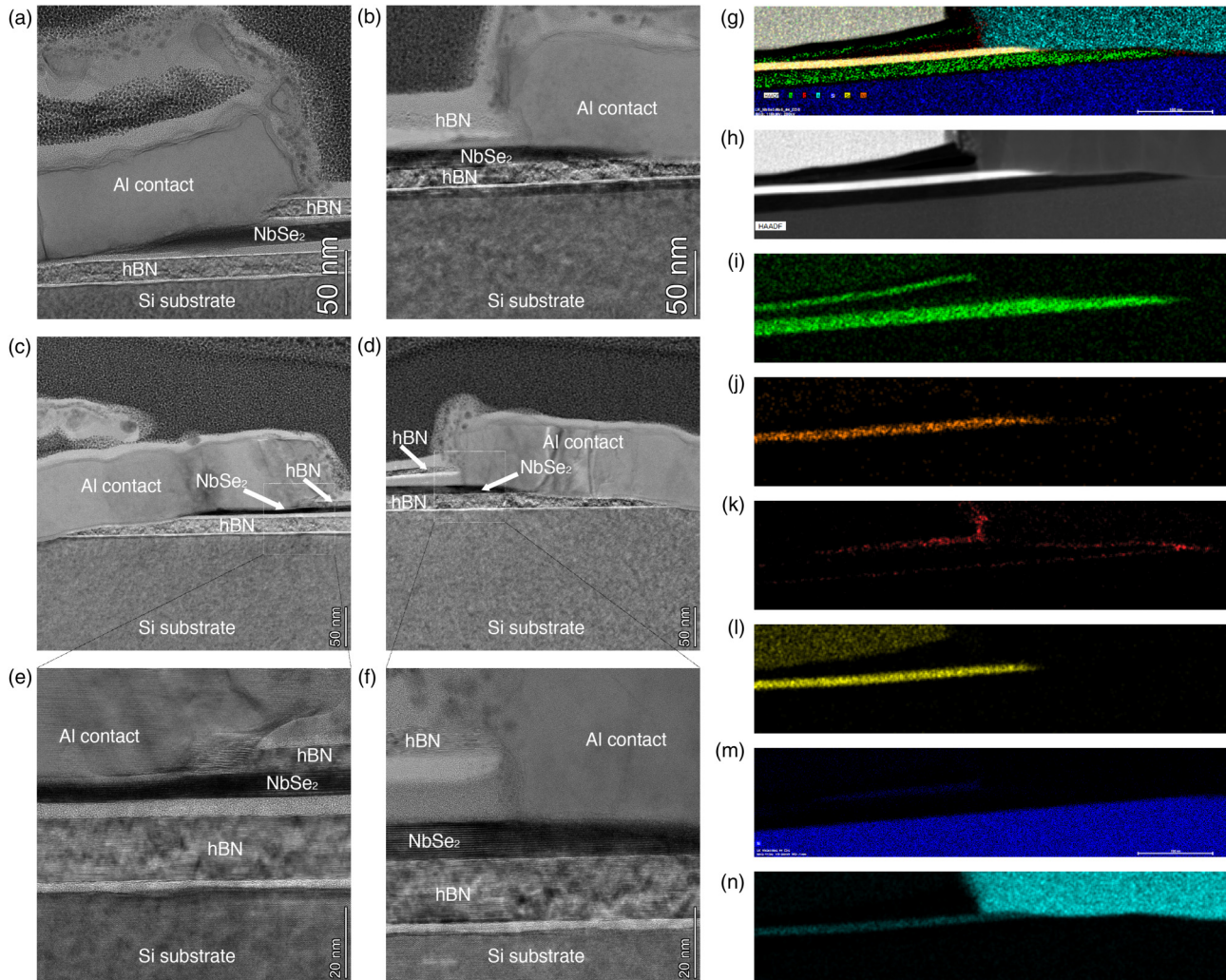


FIG. 8. STEM images of the contacts for devices F/G and false-color EDS and HAADF maps of device G used to produce Figs. 1(b) and 1(c). (a) 56.5  $\mu\text{A}$  and (b) 78.5  $\mu\text{A}$  critical current contacts of device F. (c) 128  $\mu\text{A}$  and (d) 108  $\mu\text{A}$  critical current contacts of device G. (e), (f) Detailed images of the Al/NbSe<sub>2</sub> contact regions of device G. (g) Composite EDS + HAADF map. Scale bar is 100 nm and is the same for all subfigures. (h) HAADF. (i)–(n) EDS maps of (i) nitrogen, (j) niobium, (k) oxygen, (l) selenium, (m) silicon, and (n) aluminum.

the bottom side of the color plot is sloped, showing lower temperatures are inaccessible at larger dc currents.

**APPENDIX D: STEM SPECIMEN PREPARATION AND IMAGING**

Thin lamellae from devices for scanning transmission electron microscopy (STEM) were prepared using established focused-ion beam lift-out procedures in an FEI (now Thermo Fisher Scientific) Scios focused-ion beam (FIB)/scanning electron microscope (SEM) dual beam system. First, a  $\sim 100\text{-nm}$  layer of amorphous carbon of  $15\ \mu\text{m} \times 2\ \mu\text{m}$  and then a Pt layer of  $15\ \mu\text{m} \times 2\ \mu\text{m} \times 2\ \mu\text{m}$  were deposited on the selected contact area using a focused-ion beam to protect the sample surface from ion damaging during milling; then the surrounding materials around the protected region were milled

away using a 30-kV high-current ion beam; after an initial cleaning and cut, the specimen lamellae were transferred to a Cu TEM grid; the lamellae were further thinned to  $< 100\ \text{nm}$  and further cleaned using 5- and 2-kV low-current ion beams. The final lamellae were electron transparent.

The characterization of microstructures and elemental distribution were carried out using a Thermo Fisher Scientific (formerly FEI) Titan Themis 200 G2 probe aberration-corrected field-emission transmission electron microscope equipped with a SuperX EDS (x-ray energy dispersive spectrometer) and operated at an accelerating voltage of 200 kV. STEM images were acquired at a convergence angle of 21.5 mrad with a Fischione high-angle annular dark-field (HAADF)-STEM detector. A drift correction was applied to correct for specimen drift during EDS mapping collection. (See Fig. 8.)



- [1] M. H. Devoret and R. J. Schoelkopf, Superconducting circuits for quantum information: An outlook, *Science* **339**, 1169 (2013).
- [2] M. H. Devoret and J. M. Martinis, Implementing qubits with superconducting integrated circuits, *Quantum Inf. Process.* **3**, 163 (2004).
- [3] L. J. Zeng, S. Nik, T. Greibe, P. Krantz, C. M. Wilson, P. Delsing, and E. Olsson, Direct observation of the thickness distribution of ultra thin  $\text{AlO}_x$  barriers in  $\text{Al}/\text{AlO}_x/\text{Al}$  Josephson junctions, *J. Phys. D* **48**, 395308 (2015).
- [4] I. M. Pop, T. Fournier, T. Crozes, F. Lecocq, I. Matie, B. Pannetier, O. Buisson, and W. Guichard, Fabrication of stable and reproducible sub-micron tunnel junctions, *J. Vac. Sci. Technol. B* **30**, 010607 (2012).
- [5] H. Scherer, T. Weimann, A. B. Zorin, and J. Niemeyer, The effect of thermal annealing on the properties of  $\text{Al}-\text{AlO}_x-\text{Al}$  single electron tunneling transistors, *J. Appl. Phys.* **90**, 2528 (2001).
- [6] N. Bergeal, R. Vijay, V. E. Manucharyan, I. Siddiqi, R. J. Schoelkopf, S. M. Girvin, and M. H. Devoret, Analog information processing at the quantum limit with a Josephson ring modulator, *Nat. Phys.* **6**, 296 (2010).
- [7] N. E. Frattini, V. V. Sivak, A. Lingenfelter, S. Shankar, and M. H. Devoret, Optimizing the Nonlinearity and Dissipation of a SNAIL Parametric Amplifier for Dynamic Range, *Phys. Rev. Appl.* **10**, 054020 (2018).
- [8] *The SQUID Handbook: Fundamentals and Technology of SQUIDS and SQUID Systems*, edited by J. Clarke and A. I. Braginski, 1st ed. (Wiley, Hoboken, NJ, 2004).
- [9] V. E. Manucharyan, J. Koch, L. I. Glazman, and M. H. Devoret, Fluxonium: Single Cooper-pair circuit free of charge offsets, *Science* **326**, 113 (2009).
- [10] I. V. Pechenezhskiy, R. A. Mencia, L. B. Nguyen, Y.-H. Lin, and V. E. Manucharyan, The superconducting quasicharge qubit, *Nature (London)* **585**, 368 (2020).
- [11] A. Gyenis, P. S. Mundada, A. Di Paolo, T. M. Hazard, X. You, D. I. Schuster, J. Koch, A. Blais, and A. A. Houck, Experimental realization of an intrinsically error-protected superconducting qubit, [arXiv:1910.07542](https://arxiv.org/abs/1910.07542).
- [12] T. M. Hazard, A. Gyenis, A. Di Paolo, A. T. Asfaw, S. A. Lyon, A. Blais, and A. A. Houck, Nanowire Superinductance Fluxonium Qubit, *Phys. Rev. Lett.* **122**, 010504 (2019).
- [13] X. Xi, Z. Wang, W. Zhao, J.-H. Park, K. T. Law, H. Berger, L. Forró, J. Shan, and K. F. Mak, Ising pairing in superconducting  $\text{NbSe}_2$  atomic layers, *Nat. Phys.* **12**, 139 (2016).
- [14] S. C. de la Barrera, M. R. Sinko, D. P. Gopalan, N. Sivasadas, K. L. Seyler, K. Watanabe, T. Taniguchi, A. W. Tsen, X. Xu, D. Xiao, and Benjamin M. Hunt, Tuning Ising superconductivity with layer and spin-orbit coupling in two-dimensional transition-metal dichalcogenides, *Nat. Commun.* **9**, 1427 (2018).
- [15] D. Pekker, C.-Y. Hou, V. E. Manucharyan, and E. Demler, Proposal for Coherent Coupling of Majorana Zero Modes and Superconducting Qubits Using the  $4\pi$  Josephson Effect, *Phys. Rev. Lett.* **111**, 107007 (2013).
- [16] J. P. T. Stenger, M. Hatridge, S. M. Frolov, and D. Pekker, Braiding quantum circuit based on the  $4\pi$  Josephson effect, *Phys. Rev. B* **99**, 035307 (2019).
- [17] J. I.-J. Wang, D. Rodan-Legrain, L. Bretheau, D. L. Campbell, B. Kannan, D. Kim, M. Kjaergaard, P. Krantz, G. O. Samach, F. Yan *et al.*, Coherent control of a hybrid superconducting circuit made with graphene-based van der Waals heterostructures, *Nat. Nanotechnol.* **14**, 120 (2019).
- [18] K.-H. Lee, S. Chakram, S. E. Kim, F. Mujid, A. Ray, H. Gao, C. Park, Y. Zhong, D. A. Muller, D. I. Schuster, and J. Park, Two-dimensional material tunnel barrier for Josephson junctions and superconducting qubits, *Nano Lett.* **19**, 8287 (2019).
- [19] M. Kim, G.-H. Park, J. Lee, J. H. Lee, J. Park, H. Lee, G.-H. Lee, and H.-J. Lee, Strong proximity Josephson coupling in vertically stacked  $\text{NbSe}_2$ -graphene- $\text{NbSe}_2$  van der Waals junctions, *Nano Lett.* **17**, 6125 (2017).
- [20] K. Kim, M. Yankowitz, B. Fallahzad, S. Kang, H. C. P. Movva, S. Huang, S. Larentis, C. M. Corbet, T. Taniguchi, K. Watanabe *et al.*, van der Waals heterostructures with high accuracy rotational alignment, *Nano Lett.* **16**, 1989 (2016).
- [21] A. W. Tsen, B. Hunt, Y. D. Kim, Z. J. Yuan, S. Jia, R. J. Cava, J. Hone, P. Kim, C. R. Dean, and A. N. Pasupathy, Nature of the quantum metal in a two-dimensional crystalline superconductor, *Nat. Phys.* **12**, 208 (2016).
- [22] L. Wang, I. Meric, P. Y. Huang, Q. Gao, Y. Gao, H. Tran, T. Taniguchi, K. Watanabe, L. M. Campos, D. A. Muller *et al.*, One-dimensional electrical contact to a two-dimensional material, *Science* **342**, 614 (2013).
- [23] See Supplemental Material at <http://link.aps.org/supplemental/10.1103/PhysRevMaterials.5.014001> for additional information about the devices.
- [24] J. Pearl, Current distribution in superconducting films carrying quantized fluxoids, *Appl. Phys. Lett.* **5**, 65 (1964).
- [25] J. J. Finley and B. S. Deaver, Measurements of the penetration depth in the superconducting layer crystals  $\text{NbSe}_2$  and  $\text{TaS}_2$  (pyridine)<sub>12</sub>, *Solid State Commun.* **36**, 493 (1980).
- [26] D. Vasyukov, Y. Anahory, L. Embon, D. Halbertal, J. Cuppens, L. Neeman, A. Finkler, Y. Segev, Y. Myasoedov, M. L. Rappaport *et al.*, A scanning superconducting quantum interference device with single electron spin sensitivity, *Nat. Nanotechnol.* **8**, 639 (2013).
- [27] N. F. Q. Yuan, K. F. Mak, and K. Law, Possible Topological Superconducting Phases of  $\text{MoS}_2$ , *Phys. Rev. Lett.* **113**, 097001 (2014).
- [28] Y.-T. Hsu, A. Vaezi, M. H. Fischer, and E.-A. Kim, Topological superconductivity in monolayer transition metal dichalcogenides, *Nat. Commun.* **8**, 14985 (2017).
- [29] A. Hamill, B. Heischmidt, E. Sohn, D. Shaffer, K.-T. Tsai, X. Zhang, X. Xi, A. Suslov, H. Berger, L. Forró *et al.*, Unexpected two-fold symmetric superconductivity in few-layer  $\text{NbSe}_2$ , [arXiv:2004.02999](https://arxiv.org/abs/2004.02999).
- [30] D. J. Van Harlingen, Phase-sensitive tests of the symmetry of the pairing state in the high-temperature superconductors—Evidence for  $d_{x^2-y^2}$  symmetry, *Rev. Mod. Phys.* **67**, 515 (1995).
- [31] D. Pekker, A. Bezryadin, D. S. Hopkins, and P. M. Goldbart, Operation of a superconducting nanowire quantum interference device with mesoscopic leads, *Phys. Rev. B* **72**, 104517 (2005).
- [32] L. Spietz, J. Teufel, and R. J. Schoelkopf, A twisted pair cryogenic filter, [arXiv:cond-mat/0601316](https://arxiv.org/abs/cond-mat/0601316).

- [33] Y. Chong, W. Song, M. Rehman, and S.-W. Ryu, Transmission properties of cryogenic twisted pair filters, *J. Korean Phys. Soc.* **57**, 1490 (2010).
- [34] H. Bluhm and K. A. Moler, Dissipative cryogenic filters with zero dc resistance, *Rev. Sci. Instrum.* **79**, 014703 (2008).
- [35] S. Mandal, T. Bautze, R. Blinder, T. Meunier, L. Saminadayar, and C. Bauerle, Efficient radio frequency filters for space constrained cryogenic setups, *Rev. Sci. Instrum.* **82**, 024704 (2011).
- [36] M. Thalmann, H.-F. Pernau, C. Strunk, E. Scheer, and T. Pietsch, Comparison of cryogenic low-pass filters, *Rev. Sci. Instrum.* **88**, 114703 (2017).